

# Off-equatorial deep cycle turbulence forced by Tropical Instability Waves in the equatorial Pacific

D. A. CHERIAN\*

*National Center for Atmospheric Research, Boulder, Colorado, USA.*

D.B. WHITT

*National Center for Atmospheric Research, Boulder, Colorado, USA.*

R. M. HOLMES

*Climate Change Research Centre, School of Mathematics and Statistics and the ARC Centre of Excellence for Climate Extremes, University of New South Wales, Sydney, NSW, Australia*

R.C. LIEN

*Applied Physics Laboratory, and School of Oceanography, University of Washington, Seattle, Washington*

S. D. BACHMAN

*National Center for Atmospheric Research, Boulder, Colorado, USA.*

W.L. LARGE

*National Center for Atmospheric Research, Boulder, Colorado, USA.*

## ABSTRACT

The equatorial Pacific cold tongue is a site of large heat absorption by the ocean. This heat uptake is enhanced by a daily cycle of turbulence beneath the mixed layer (deep-cycle turbulence) that removes heat from the sea surface and deposits it in the upper flank of the Equatorial Undercurrent. Deep-cycle turbulence results when turbulence is triggered daily in sheared and stratified flow that is marginally stable (gradient Richardson number  $Ri \approx 0.25$ ). Deep-cycle turbulence has been observed on numerous occasions in the cold tongue at  $0^\circ\text{N}$ ,  $140^\circ\text{W}$ , and may be modulated by Tropical Instability Waves (TIWs). Here we use a primitive equation regional simulation of the cold tongue to show that deep-cycle turbulence can also occur off the equator within the cold cusps of TIWs where the flow is marginally stable. In the cold cusp, pre-existing equatorial zonal shear  $u_z$  is enhanced by horizontal vortex stretching near the equator, and subsequently modified by horizontal vortex tilting terms to generate meridional shear  $v_z$  off the equator. Turbulence in the sheared flow of the cold cusp is triggered daily by the descent of the surface mixing layer associated with the weakening of the stabilizing surface buoyancy flux in the afternoon. Observational evidence for off-equatorial deep-cycle turbulence is restricted to a few CTD casts, which when combined with shear from shipboard ADCP data suggest the presence of marginally stable flow in TIW cold cusps. This study motivates further observational campaigns to characterize the modulation of deep-cycle turbulence by TIWs both on and off the equator.

## 1. Introduction

The equatorial Pacific cold tongue is a zonal band of cold upper-ocean water in the eastern equatorial Pacific extending between the Pacific's eastern margin and approximately  $155^\circ\text{W}$ . Being cold water in a region of large solar insolation, the cold tongue is a region of large heat ab-

sorption by the ocean between approximately  $3^\circ\text{S}$  and  $3^\circ\text{N}$  (for example Large and Yeager 2009; Holmes et al. 2019). Absorbing such a large amount of heat while maintaining cold sea surface temperatures (SSTs) is only possible if the heat taken in by the ocean is quickly transported away from the equatorial sea surface. Mixed layer heat budgets for the eastern Pacific constructed using equatorial mooring observations show that the downward transport of heat by microscale turbulence is essential to keeping the sea surface cool (Moum et al. 2013; Wang and McPhaden

\*Corresponding author address: Deepak A. Cherian, NCAR, P.O. Box 3000, Boulder, CO 80307-3000.  
E-mail: deepak@cherian.net

1999, 2000; Warner and Moum 2019; Ray et al. 2018). The annual cycle of turbulence is strong enough that there is only a single peak in the annual cycle of equatorial sea surface temperature (SST) despite a double peak in solar insolation as the sun “crosses” the equator twice through the year (Moum et al. 2013). On longer timescales, the rate of change of SST during ENSO phase transitions is seen to approximately agree with both amplitude and phase of turbulence heat flux divergence across the mixed layer (Warner and Moum 2019). Equatorial mixing might be critical to one of the Earth’s most consequential climate phenomena and yet little is known about its spatial structure with current observations restricted to a few sites along the Equator.

The microstructure observations that do exist have illustrated the complex nature of equatorial turbulence. At the equator, winds maintain a strong zonal mean flow with intense vertical shear between the eastward flowing Equatorial Undercurrent (EUC) at depth and the westward flowing near-surface South Equatorial Current (SEC). Observations at  $0^{\circ}\text{N}$ ,  $140^{\circ}\text{W}$  repeatedly show the existence of a deep-reaching daily cycle of shear-driven turbulence — the “deep cycle of turbulence” — in the high shear zone above the core of the EUC but beneath the base of the mixed layer (Gregg et al. 1985; Moum and Caldwell 1985; Lien et al. 1995; Moum et al. 2009). In this deep-cycle layer the flow’s gradient Richardson number,

$$\text{Ri} = b_z / (u_z^2 + v_z^2), \quad (1)$$

where  $b = -g\rho/\rho_0$  is buoyancy,  $u$  and  $v$  are the horizontal components of velocity and subscripts indicate differentiation, remains near its critical value of 0.25 throughout the year. That is, this layer is marginally stable to shear instability (Thorpe and Liu 2009; Smyth and Moum 2013; Pham et al. 2017; Smyth et al. 2019). A daily cycle of turbulence requires a diurnal trigger in the marginally stable layer. At least two hypotheses have been proposed for this diurnal trigger. A number of authors (e.g. Wijsseker and Dillon 1991; Peters et al. 1994) propose that downward-propagating internal waves, excited at the base of the mixed layer during nighttime convection, break in the marginally stable layer and trigger turbulence. More recently, (Pham et al. 2017) propose that the diurnal trigger is the instability of the diurnal warm-layer jet formed by the trapping of momentum in a near-surface stratified layer. As the near-surface stratification built up by solar radiation during the day decreases in the afternoon the warm-layer jet goes unstable, triggering turbulence at the base of the mixed layer (Pham et al. 2017). This turbulence transports momentum downward, locally increasing shear in the marginally stable layer, reducing Ri and triggering further shear instability. As this process continues,

the envelope of actively turbulent fluid propagates downward and is visible as a downward descent of a local maximum in vertical shear (Smyth et al. 2013). Turbulence persists during the next morning at depths up to 80–100 m at  $0^{\circ}\text{N}$ ,  $140^{\circ}\text{W}$  despite the cessation of near-surface convection; and increases Ri back to its marginally stable value of approximately 0.25 at which point turbulence decays (Smyth et al. 2019) argue that turbulent diffusion tends to reduce buoyancy and velocity gradients,  $b_z$  and  $u_z$ , at roughly similar rates so  $\text{Ri} = b_z/u_z^2$  must increase). In this way flow in the deep-cycle layer is restored to a state of marginal stability ( $\text{Ri} \approx 0.25$ ). Near-surface turbulence is then triggered in the late afternoon and the cycle repeats. Large eddy simulations initialized with mean fields representative of each of the four seasons show that the deep cycle exists throughout the year, though the depth to which it penetrates varies with the seasonal shoaling and deepening of the EUC (Pham et al. 2017). Mooring observations in the Atlantic Ocean (Wenegrat and McPhaden 2015), ship-based microstructure measurements in the Indian Ocean (Pujiana et al. 2018), and a global primitive equation simulation using a k-epsilon turbulence closure model (Pei et al. 2020) suggest that deep-cycle turbulence may also exist in the equatorial Atlantic and Indian Oceans. Most previous studies have focused only on deep-cycle turbulence on the Equator.

Equatorial turbulence is also modulated by mesoscale variability in the form of Tropical Instability Waves (TIWs). TIWs are formed through barotropic and baroclinic instability of the equatorial current system, and manifest as a series of westward travelling cold cusps and warm troughs. TIWs have zonal wavelengths of 1000–2000 km, periods of 15–40 days and propagate westward with a phase speed of approximately  $0.5 \text{ m s}^{-1}$  (Philander 1976; Legeckis 1977; Qiao and Weisberg 1995; Chelton et al. 2000; Lyman et al. 2005; Holmes and Thomas 2016). The cold cusps of TIWs exhibit vigorous circulation features with sharp fronts and convergence zones that influence biological activity (Yoder et al. 1994; Strutton et al. 2001; Warner et al. 2018).

TIWs may modulate cold tongue turbulence. Lien et al. (2008) reported intense mixing at the base of the mixed layer recorded by a Lagrangian float that meandered through two TIWs between  $2^{\circ}\text{S}$  and  $1^{\circ}\text{N}$  in 2005 with a peak heat flux estimate of  $1000 \text{ W m}^{-2}$ . During the EQUIX experiment at  $(0, 140^{\circ}\text{W})$  in 2008, a La Niña year, turbulent heat fluxes at the equator reached  $400 \text{ W m}^{-2}$  when averaged over two weeks (Moum et al. 2009) in the presence of TIWs, compared to the approximately  $50 \text{ W m}^{-2}$  measured previously (Lien et al. 1995). The base of the marginally stable layer appears to shallow by a factor of two to 50 m during the warm phase of the TIW as compared to that during the cold phase (Moum et al. 2009;

Inoue et al. 2012, 2019). Recent work with TAO observations indicates that a subsurface mode of TIWs (Liu et al. 2019) as well as equatorial inertial gravity waves at periods between 3 and 25 days (Liu et al. 2020) may strongly influence the vertical structure of shear and thereby diapycnal mixing at the equator, consistent with (Moum et al. 2009; Inoue et al. 2019). Note that microstructure profiler observations have not yet captured one entire TIW period. These observations are consistent with modeling studies that show enhanced turbulence both at the equator during particular TIW phases (Menkes et al. 2006; Holmes and Thomas 2015). Holmes and Thomas (2015) proposed a dynamical explanation for the enhancement of equatorial turbulence by TIWs: meridional diffusivity (positive  $v_y$ ) of TIW flow at the equator during the cold phase stretches the southward-oriented meridional component of horizontal vorticity ( $\omega^y = w_x - u_z$ ). The stretching increases  $|\omega^y|$ , intensifies the pre-existing EUC shear  $u_z$  at the equator, and forces intense turbulence. During the warm phase, the reverse happens: vortex tubes are squashed and  $u_z$  weakens with a corresponding weakening of turbulence. Observational evidence for this mechanism is inconclusive, due in part to the difficulty in obtaining observations of  $v_y$  (Inoue et al. 2019). TIWs also change the latitudinal scale of equatorial mixing: the simulations of both Menkes et al. (2006) and Holmes and Thomas (2015) show the presence of intense mixing in TIW cold cusps off the equator. But, most equatorial microstructure measurements have been made right at the equator, primarily at  $0^\circ$ ,  $140^\circ\text{W}$  in the Pacific. This sampling bias means that large unknowns remain in our knowledge of the spatial distribution of equatorial upper-ocean mixing.

Here we use a  $1/20^\circ$  regional model of the cold tongue to study how TIWs modulate turbulence off the equator. The simulated TIWs force off-equatorial marginally stable flow and deep-cycle turbulence by generating intense meridional shear ( $v_z$ ) in the eastward extension of a TIW's cold cusp (Sections 3 and 4). This shear results from the rotation or tilting of horizontal vorticity generated by horizontal vortex stretching at the equator (Section 4b). Indirect observational evidence for this TIW-forced off-equatorial deep cycle is presented through  $Ri$  profiles from three cruise sections through TIWs at  $110^\circ\text{W}$  (Section 5). Our results emphasize the need to observe turbulence variability off the equator; to validate the results presented here, to assess the accuracy of turbulence parameterization schemes in simulating deep-cycle turbulence modulated by TIWs, and to fully characterize the role of deep-cycle turbulence in the heat budget of the cold tongue.

## 2. Methods

### a. Model configuration

We use a regional configuration of the MITgcm (Marshall et al. 1997; Adcroft et al. 2004) to model the equatorial Pacific cold tongue using NCAR's Cheyenne cluster (Computational And Information Systems Laboratory 2019). The domain extends from  $170^\circ\text{W}$  to  $95^\circ\text{W}$ ,  $12^\circ\text{S}$  to  $12^\circ\text{N}$  with a horizontal grid spacing of  $1/20^\circ$ . There are 345 vertical levels with a spacing of 1m in the top 250m that increases to a maximum of 250m. The model is forced at the surface with fields from the JRA-55do reanalysis (Tsujino et al. 2018) and lateral boundary conditions are specified using daily averaged fields from the Mercator GLO-RYS12V1  $1/12^\circ$  ocean reanalysis product (Copernicus identifier GLOBAL\_REANALYSIS\_PHY\_001\_030). The simulated time period is from 01 Sep 1995 to 28 Feb 1997. There is no tidal forcing. The time axis, when presented in figures, is “local time” at  $110^\circ\text{W}$  chosen to be UTC-7.

Sub-grid scale vertical mixing is parameterized using the K Profile Parametrization (KPP) scheme of Large et al. (1994) with standard parameter values (Large and Gent 1999). The KPP turbulence scheme divides the water column into three parts: an interior region, a boundary layer, and a surface layer (defined to be the top 10% of the boundary layer near the surface). The KPP boundary layer depth  $H_{\text{KPP}}$  is usually chosen as the depth at which the *bulk* Richardson number

$$Ri_b = \frac{\Delta b H_{0.3}}{|\Delta V|^2 + V_t^2(H_{0.3})} \quad (2)$$

exceeds a critical value chosen to be 0.3 ( $H_{0.3}$ ). Here  $\Delta b$  and  $\Delta V$  are the differences between values of resolved buoyancy  $b$  and resolved velocity  $V$  at the surface and at the base of the boundary layer  $z = H_{0.3}$ .  $V_t$  represents a parameterized velocity due to unresolved turbulent eddies. In addition,  $H_{\text{KPP}}$  is restricted to be less than the Monin-Obukhov length scale

$$L_{MO} = \frac{-u_*^3}{\kappa B_0} \quad (3)$$

so that

$$H_{\text{KPP}} = \min [L_{MO}, H_{0.3}] \quad (4)$$

Here  $u_* = \sqrt{\tau/\rho_0}$  is the friction velocity where  $\tau$  is the wind stress,  $B_0$  is the surface buoyancy flux, and  $\kappa = 0.4$  is the von Karman constant. Below  $H_{\text{KPP}}$ , diffusion due to shear instabilities is parameterized using a diffusivity that is a smooth function of gradient Richardson number  $Ri$ . This function is non-zero for  $Ri < 0.7$  (Large et al. 1994, their Figure 3). The shear mixing scheme's parameters were specifically tuned to reproduce the onset of nighttime convection relative to LES (Large and Gent 1999).

### b. Model Validation

The model simulates the equatorial Pacific reasonably well (Figure 1). The model fields are compared with the Johnson et al. (2002) climatology and an annual mean climatology constructed using TAO mooring observations in the 1990–2000 decade at 110° W. At the equator, the EUC maximum is approximately 15–20 m deeper than the TAO data and the Johnson et al. (2002) climatology (Figure 1b), though the depth-integrated zonal velocity in the top 250 m is comparable to that from the Johnson climatology (Figure 1c). There is a subsurface warm bias relative to both observational datasets (Figure 1a, e). This subsurface warm bias extends from about 6°S and 6° N, where the top 75 m are slightly less stratified in temperature than observed.

### c. Diagnostics

All derivatives in presented terms are estimated using centered differences.  $Ri$  is masked out when  $N^2 < 10^{-6} \text{ s}^{-2}$  or  $S^2 < 10^{-6} \text{ s}^{-2}$ . The mixed layer depth  $z_{MLD}$  is computed as the shallowest depth at which the density exceeds the surface density by  $0.015 \text{ kg m}^{-3}$ . The base of the deep cycle layer  $z_{Ri}$  is computed as the shallowest depth below the mixed layer base when  $Ri$  exceeds 0.5. Our choice of 0.5 instead of 0.25 is discussed in Section 3. The thickness of the low Richardson number layer or “low  $Ri$  layer” is defined as  $H = z_{MLD} - z_{Ri}$ . The parameterized turbulent heat flux  $J_q^t = -\rho_0 c_p K_T (T_z - \gamma_T)$  where  $c_p$  is the specific heat capacity of water,  $\gamma_T$  is a non-local transport that is non-zero only during convective forcing conditions (Large et al. 1994, their equations 19, 20). Negative values of  $J_q^t$  indicate heat moving downward.

## 3. TIW modulated turbulence in the cold tongue

TIW variability imprints itself strongly on SST, surface heat fluxes, and subsurface turbulent mixing both on and off the equator (Figure 2). The cold tongue, structured by TIW cold cusps, is characterized by strong heat absorption at the surface (positive  $Q_{net}$  in Figure 2a) and intense downward turbulent heat fluxes in the thermocline (Figure 2d). The low  $Ri$  layer also coincides with the cold tongue suggesting both TIW influence and the existence of intense vertical mixing (Figure 2e). In contrast, the EUC does not coincide with the cold tongue; it is concentrated in an approximately 1° wide latitudinal band around the equator, particularly to the east of 125° W (Figure 2c). The off-equatorial low  $Ri$  flow (Figure 2e) and associated turbulent heat fluxes (Figure 2d) cannot be directly associated with shear in the EUC.

Though this manuscript subsequently focuses on one particular TIW to elucidate the processes driving the turbulent heat fluxes below the cold tongue, the correlation between low  $Ri$  flow off the equator and cold SSTs asso-

ciated with TIWs is visible throughout the simulation at 110°W, 125°W, 140°W and 155°W. (Figure 3). Low  $Ri$  values are more common north of the equator than south of the equator, and the latitudinal extent of low  $Ri$  flow widens toward the west. These patterns match those of SST and are seen outside the latitudinal extent of the EUC (black lines in Figure 3). Later during the season (Jan-Mar) TIW amplitudes weaken and clear cusps are not visible in SST. Even then low  $Ri$  values are still visible off the equator where relatively cold SSTs are present (e.g. at 110°W in March; Figure 3a,b) These patterns are qualitatively similar to those in Figure 2d,e. The rest of this manuscript focuses on one representative TIW highlighted by the black box in Figure 2d.

The vertical structure of mixing associated with this particular TIW at 110°W (black box in Fig. 2d) shows a deep cycle of mixing both on and off the equator at 3.5°N (Figure 4c,e). At both latitudes, there is a daily cycle in the parameterized turbulent heat flux beneath the mixed layer base ( $z_{MLD}$ ; orange line in Figure 2c,e) and above the base of the low  $Ri$  layer ( $z_{Ri}$ ; black line in Figure 2c,e). At the equator,  $z_{Ri}$  shallows during the TIW warm phase as observed and described by Inoue et al. (2012, 2019) and Moum et al. (2009). At 3.5°N, the deep cycles start when the cold cusp reaches that latitude (around Nov. 26), and persist over the approximately two week time period during which the TIW cold cusp reaches this latitude. There is almost no turbulence beneath the mixed layer prior to the arrival of the cold cusp and after its departure. Daily cycles are also visible in  $Ri$ ,  $S^2$ ,  $N^2$  at 3.5°N beneath the mixed layer base for the time period when the deep cycle is active (Figure 5). Such daily cycles in shear, stratification and  $Ri$  are qualitatively similar to observations and LES at 0°N, 140°W (Moum et al. 2009; Pham et al. 2017).

A robust feature of observed deep cycle layers at the equator is a median  $Ri$  of 0.25 (Smyth and Moum 2013; Pham et al. 2017). In the simulated deep cycle layer both on and off the equator,  $Ri$  is indeed low, similar to observations, but the median value is higher at about 0.4, a notable bias (Figure 4d,f), suggesting that the KPP mixing scheme is too diffusive. This may be partly responsible for the subsurface warm bias in Figure 1e. The critical  $Ri$  bias may partly arise because KPP’s shear mixing scheme parameterizes diffusivity  $K_T$  as a smooth function of  $Ri$  that is non-zero for  $Ri < 0.7$  (Large et al. 1994). This function lacks a rapid transition in diffusivity as  $Ri$  reduces, thereby making it difficult to represent a state of marginal instability at  $Ri \approx 0.25$  (Holmes and Thomas 2015). In contrast, plots of diffusivity versus  $Ri$  from observations show a steeper dependence (for example, Zaron and Moum 2009; Peters et al. 1988). We also find that approximately a third of the parameterized turbulent heat flux in the deep cycle layer is handled by KPP’s surface layer mixing scheme (discussed later in Section d). Hence deficiencies in KPP’s

shear mixing scheme may not be the sole reason for the bias in  $Ri$ . Here we account for the bias in  $Ri$  by treating simulated flows with  $Ri \approx 0.4$  as being marginally stable.

#### 4. Dynamics of off-equatorial deep-cycle turbulence

A deep cycle of turbulence can only exist in equilibrium in a stratified fluid given a continuous source of shear that acts to reduce  $Ri$ ; a diurnal trigger that initiates turbulence daily which may then increase  $Ri$  (Smyth et al. 2019); and a process that maintains stratification within the deep cycle layer. Together these act to maintain the stratified deep-cycle layer in a state of marginal stability. At  $0^\circ$ ,  $140^\circ\text{W}$  equatorial winds maintain intense zonal shear  $u_z$  between the SEC and the EUC and the diurnal trigger may be the nighttime instability of the surface-trapped diurnal warm-layer jet (Pham et al. 2017) or the breaking of downward propagating internal waves triggered by nighttime convection (Wijesekera and Dillon 1991). In contrast, we will see that the simulated marginally stable flow and deep cycle turbulence at  $3.5^\circ\text{N}$ ,  $110^\circ\text{W}$  is forced by TIW meridional shear  $v_z$  (Sections 4a, 4b) and the diurnal trigger is the daily descent of the surface mixing layer associated with the weakening of the stabilizing surface buoyancy flux in the afternoon (Section 4d). We begin by describing the shear and stratification structure in the simulated off-equatorial deep-cycle (Section 4a).

##### a. Marginal stability, shear and stratification in the cold cusp

The off-equatorial low  $Ri$  layer is closely associated with the TIW's cold cusp (Figure 6a,b, also Figure 2b,d,e and Figure 3). The contributions of each vector component of the shear as well as the stratification to  $Ri$  in the low- $Ri$  layer below the cold cusp are decomposed and illustrated by reduced shear  $\text{Sh}_{\text{red}}^2 = (u_z^2 + v_z^2) - N^2/Ri_c \gtrsim 0$  (Figure 6c), where  $Ri_c = 0.4$  instead of the usual 0.25 following the discussion in Section 3. The flow in much of the cold cusp is near marginal stability, though the components of  $\text{Sh}_{\text{red}}^2$  vary considerably in space and time.

Between  $1^\circ\text{S}$  and  $2^\circ\text{N}$  and behind the cold cusp, the vertical shear of the flow is largely associated with  $u_z$  (Figure 6d). North of  $2^\circ\text{N}$ , the shear is largely associated with  $v_z$  (Figure 6e). Combining the shear fields (Figure 6d,e) with the map of low  $Ri$  layer thickness and  $\text{Sh}_{\text{red}}^2$  (Figure 6b,c) suggests that  $u_z$  drives the flow toward marginal instability south of  $2^\circ\text{N}$  while  $v_z$  drives the flow toward marginal instability north of  $2^\circ\text{N}$ , in the eastward extension of the cold cusp. Since  $\text{Sh}_{\text{red}}^2$  is a linear combination of contributions from  $N^2$ ,  $u_z^2$  and  $v_z^2$ , we split  $\text{Sh}_{\text{red}}^2$  into two terms to evaluate whether  $u_z$  or  $v_z$  is individually large enough to overcome half the stratification necessary to drive the flow

toward marginal stability,

$$\text{Sh}_{\text{red}}^2 = \left[ u_z^2 - \frac{N^2}{2Ri_c} \right] + \left[ v_z^2 - \frac{N^2}{2Ri_c} \right]. \quad (5)$$

Snapshots of heat flux  $J_q$ , reduced shear  $u_z^2 + v_z^2 - N^2/Ri_c$  and the two terms on the RHS of (5) computed using  $Ri_c = 0.4$  are shown in Figure 7a–l at three different times indicated by vertical dashed lines in Figure 6. Enhanced turbulence is present in the low  $Ri$  layer between  $z_{\text{MLD}}$  (orange) and  $z_{\text{RI}}$  (black). The regions of enhanced turbulence coincide with positive values of reduced shear. Zonal shear  $u_z$  is responsible for shear turbulence both at the equator (Figure 7c,g,k) and in the northward-oriented cold cusp between  $0$  and  $3^\circ\text{N}$  (Figure 7f,g). The corresponding  $v_z$  is weak (Figure 7h,i). This pattern reverses in the eastward extension of the cold cusp:  $v_z$  is strong but  $u_z$  is weak between  $2^\circ\text{N}$  and  $4^\circ\text{N}$  (Figure 7k,l). These three cross-sections confirm that  $u_z$  acts to force turbulence in the near-equatorial region ( $1^\circ\text{S}$ – $2^\circ\text{N}$ ) while  $v_z$  forces the off-equatorial deep cycle turbulence, as inferred from Figure 6c,d,e.

The stratification  $N^2$  in the low- $Ri$  layer below the cold cusp varies by approximately a factor of two between the equator and the eastward extension of the cold cusp (Figure 6f, Figure 10a). This variation is a result of intense mixing seen in the cold cusp as we show later. Next we examine the dynamics underlying the shear field.

##### b. Shear forcing of off-equatorial deep cycle turbulence

The enhanced off-equatorial  $v_z$  is a consequence of the rotation of the horizontal vorticity vector by the TIW's off-equatorial flow (Figure 8). Although the flow is unsteady, water parcels follow a vortex-like circular path between  $1^\circ\text{N}$  and  $4^\circ\text{N}$  in the cold cusp (Dutrieux et al. 2008; Holmes et al. 2014) illustrated by streamlines (green) calculated using velocities relative to an approximate TIW westward translation speed of  $0.5 \text{ m s}^{-1}$  (determined from Hovmöller plots of SST and 0–60m depth-averaged  $v$  at latitudes between  $0$  and  $4^\circ\text{N}$ ) Near-equatorial disturbances propagate faster than off-equatorial disturbances (Kennan and Flament 2000) so the streamlines may be a poor representation of pathlines there. Streamlines pass through the near-equatorial region of high zonal shear, then move northward and eastward approximately parallel to the SST front (black contour;  $23.8^\circ\text{C}$ ). During this transit the horizontal vorticity vector  $\omega^x\hat{i} + \omega^y\hat{j} = (w_y - v_z)\hat{i} + (u_z - w_x)\hat{j}$  (black) rotates from pointing southward to pointing westward. This rotation suggests that horizontal vortex tilting transforms  $\omega^y$  to  $\omega^x$  during the parcel's transit i.e. negative  $u_z$  in the near-equatorial region is rotated to become positive  $v_z$  off the equator.

The dynamics of this transformation can be quantified using the evolution equation for the two shear components.

These equations are written so that the tilting term is decomposed into two terms,

$$D_t u_z = \underbrace{+u_z v_y}_{\text{STRETCH}} + \underbrace{\zeta v_z}_{\text{TILT1}} - \underbrace{v_x v_z}_{\text{TILT2}} - \underbrace{b_x + F_z^x}_{\text{BUOY FRIC}} \quad (6)$$

$$D_t v_z = +v_z u_x - \zeta u_z - u_y u_z - b_y + F_z^y. \quad (7)$$

Here  $\zeta = (f + v_x - u_y)$  is the absolute vertical vorticity,  $b_x, b_y$  are baroclinic torque terms,  $F_z^x, F_z^y$  are the frictional terms, and  $D_t = \partial_t + \partial_x + \partial_y + \partial_z$  is the material derivative. The decomposition of the tilting terms is useful because  $\zeta \approx 0$  in the cold cusp (Holmes et al. 2014). We present both components of vertical shear as well as the evolution terms in the RHS of equations (6) and (7), averaged over the top 60 m, in Figure 9 along with a contour marking a low  $Ri$  layer thickness of 30 m for reference. We focus on the magnitudes of the evolution terms within this 30m low  $Ri$  layer thickness contour. In the northward-oriented cold cusp between 0° and 3°N, TIW meridional diffusance (positive  $v_y$ ) acts to stretch the horizontal vorticity through the stretching term,  $u_z v_y$  (Figure 9c), intensifying  $u_z$  and forcing turbulence (Figure 7e-h) as described by Holmes and Thomas (2015). North of approximately 2°N, the zonal shear weakens and meridional shear intensifies as the horizontal vorticity vector rotates from pointing southward to pointing westward. That is, negative  $u_z$  is converted to positive  $v_z$  in the northwest corner of the TIW (Figure 8) through the horizontal vortex tilting terms for both  $u_z$  and  $v_z$  (TILT2, Figure 9g,h). The sign of the TILT2 tilting terms within the 30 m contour is such that  $u_z$  is increased from a negative value to 0 (its magnitude is decreased) while  $v_z$  is increased from 0 to a positive value (Figure 9a,b). Both tilting by absolute vertical vorticity (TILT1, Figure 9e,f) and the baroclinic torque (BUOY, Figure 9i,j) are relatively weak within the 30m low  $Ri$  layer thickness contour. The TILT2 terms in equations (6) and (7) do not simply rotate pre-existing shear but also act to change the shear magnitude squared  $S^2$  (horizontal enstrophy) as is seen by constructing an equation for the evolution of  $S^2$

$$\frac{1}{2} D_t S^2 = \underbrace{u_z^2 v_y + v_z^2 u_x}_{\text{STRETCH}} - \underbrace{(u_y + v_x) u_z v_z}_{\text{TILT2}} - \underbrace{u_z b_x - v_z b_y}_{\text{BUOY}} + \underbrace{u_z F_z^x + v_z F_z^y}_{\text{FRIC}} \quad (8)$$

Taken together, the stretching and TILT2 terms in (8) act to increase  $S^2$  throughout the deep cycle layer (not shown); here the TILT2 terms appear as flow deformation in the  $x - y$  plane acting to stretch horizontal vortex lines in that plane, thereby changing horizontal vorticity and vertical shear. Enhanced turbulence within the 30 m low  $Ri$  layer thickness contour acts to decrease  $S^2$  (Figure 9k,l). The intensification of  $u_z$  in a near-equatorial region by horizontal vortex stretching (Holmes and Thomas 2015), the subsequent rotation of  $u_z$  to  $v_z$ , or  $\omega^y$  to  $\omega^x$ , by the anticyclonic TIW flow  $u_y$  (Figure 9g,h), and the intensification

of shear through flow deformation is the continuous shear forcing that forces the turbulent mixing in the deep-cycle layer below the cold cusp.

### c. Stratification in the cold cusp

Stratification  $N^2$  in the low- $Ri$  layer decreases as water parcels flow northward and then eastward along the cold cusp (Figure 6f, Figure 10a). Consider the evolution equation for  $N^2$ , ignoring lateral mixing,

$$D_t N^2 = D_t b_z = \underbrace{-u_z b_x - v_z b_y}_{\text{TILT}} - \underbrace{w_z b_z}_{\text{STRETCH}} + \underbrace{\partial_{zz} K_T b_z}_{\text{MIX}}. \quad (9)$$

Integrated over the low  $Ri$  layer, the stretching and tilting terms act to increase stratification (STRETCH + TILT, Figure 10c) while the mixing acts to decrease stratification (MIX, Figure 10d). In total, these terms act to decrease stratification within most of the low  $Ri$  layer (Figure 10b). Consequently, a relatively weaker shear field can force turbulence in the cold cusp off the equator than on the equator, where stratification is stronger.

### d. Simulated trigger of deep cycle turbulence

As at the equator, turbulence in the low  $Ri$  layer must be triggered daily for a diurnal cycle to exist (Figure 5). How does the KPP scheme model that daily trigger off the equator?

During times of TIW influence, our simulations show some diurnal variation in  $H_{0.3}$ , the shallowest depth at which  $Ri_b = 0.3$  (Section a), in the TIW cold cusp off the equator (Figure 11). However the base of the KPP boundary layer  $H_{\text{KPP}}$  is significantly shallower than  $H_{0.3}$  during daytime (compare black and thick red lines in Figure 11). During daytime, the surface buoyancy forcing is stabilizing and values of  $H_{\text{KPP}}$  are limited to the Monin Obukhov scale  $L_{MO}$  (Section a) which is approximately 2.5-5m (one to two grid cells deep). After peak sun in the afternoon,  $L_{MO}$  deepens to approximately 50-60 m and so does  $H_{\text{KPP}}$  (Figure 11b-e). After 7pm, the surface heat flux turns destabilizing, so  $L_{MO}$  becomes negative, the limiter is removed and  $H_{\text{KPP}}$  matches  $H_{0.3}$  during the night. In this way, the descent of the daytime shear layer in the late afternoon (Smyth et al. 2013) is entirely modelled by the change in surface fluxes (as captured by  $L_{MO}$ ) rather than a dynamical instability resulting from increased interior shear relative to the stratification (as captured by  $H_{0.3}$ ).

Note that  $H_{\text{KPP}} = L_{MO} > z_{\text{MLD}}$  for approximately an hour (6pm-7pm) before the onset of convection (vertical white dashed lines). Diffusivities are enhanced within the boundary layer, which includes the stratified water beneath the mixed layer, resulting in large heat fluxes just prior to the onset of nighttime convection. The descent of the boundary layer results in strong parameterized

turbulence heat fluxes below the mixed layer where the strong vertical stratification combines with high boundary layer diffusivities (Figure 11e). Parameterized mixing is also excited in the low  $Ri$  layer below  $H_{KPP}$ . During the night,  $Ri$  increases which in turn reduces  $J'_q$  (Figure 11b,e). Meanwhile  $H_{KPP}$  shoals and approaches  $z_{MLD}$  as it descends. When the sun rises, the  $L_{MO}$  limiter is activated and the boundary layer shoals to its daytime value of approximately 5 m. Since  $L_{MO} < H_{0.3}$ ,  $H_{KPP}$  is set to  $L_{MO}$  during the day. Daytime  $Ri$  values in the low  $Ri$  layer are in the 0.4–0.5 range, so the parameterized shear turbulence is never completely extinguished (KPP enhances diffusivities for  $Ri < 0.7$ ). The daily cycle then repeats (Figure 5).

There are two peaks in the parameterized turbulent heat flux  $J'_q$  averaged over the passage of the entire TIW associated with deep-cycle layers at the equator and in the cold cusp (Figure 12a). Roughly one third of the total off-equatorial parameterized heat flux in the low  $Ri$  layer between 3°N and 5°N occurs within the KPP surface boundary layer (Figure 12a). In contrast, this fraction is negligible near the equator. The equatorial deep cycle is almost completely modelled by KPP's interior shear mixing scheme. The difference between the modeled equatorial and off-equatorial deep cycles is likely due to the difference in  $N^2$  (Figure 12b). Off the equator,  $N^2$  is smaller than at the equator by a factor of two to three, so  $H_{0.3}$  can penetrate deeper below the mixed layer compared to at the equator (Figure 12c). So a larger fraction of the low  $Ri$  layer off the equator is handled by the surface boundary layer scheme. Though the difference between  $H_{KPP}$  and  $z_{MLD}$  off the equator is small on average (compare orange and black lines in Figure 12c), the large diffusivities of the surface boundary layer scheme combine with small but non-zero stratification to yield large heat fluxes (e.g. Figure 11e). This difference in equatorial and off-equatorial  $N^2$  also means that the  $L_{MO}$  limiter is more consequential off the equator than at the equator. This may explain why Large and Gent (1999) did not see any sensitivity to the  $L_{MO}$  limiter in their equatorial study (though note that their calculations did not represent the influence of TIWs; their Section 3d).

## 5. Indirect observational evidence

To our knowledge there is no reported observational evidence for an off-equatorial deep cycle of turbulence associated with TIWs. In the absence of direct microstructure measurements, one might look at *in-situ*  $Ri$  estimates since marginal stability is detectable using coarse measurements of shear and stratification at least at the equator (Smyth and Moum 2013; Pham et al. 2017). The absence of ADCPs on the off-equatorial TAO moorings prevents replicating the analysis of Smyth and Moum (2013) or

Pham et al. (2017). Instead we will use coincident measurements of velocity from shipboard ADCPs and density from CTD casts obtained during cruises that sampled a TIW cold cusp by chance. Cruise CTD and ADCP data were obtained from the CLIVAR and Carbon Hydrographic Data Office (CCHDO) and the Joint Archive for Shipboard ADCP (JASADCP) respectively.

$Ri$  estimated using high resolution velocity and stratification measurements indicate that deep cycle turbulence is associated with a  $Ri$  distribution with statistical mode 0.25 (2-m velocity bins; Smyth and Moum 2013). The mode remains at 0.25 even when the velocity measurements are significantly degraded to 16-m bins. The Smyth and Moum (2013) observations are limited in that they were taken at a single location (0°N, 140°W) for a short period of time (two weeks) during a period of strong TIW forcing. Guided by their observations, we assume that deep cycle turbulence everywhere is characterized by a  $Ri$  distribution with statistical mode 0.25, and that  $Ri$  in the deep cycle layer can be estimated from relatively coarse observations. Since the mode is 0.25, we expect the most likely observed  $Ri$  value to be 0.25 in a deep cycle layer.

We infer low values of  $Ri$ , less than 1, below the mixed layer both at the equator (as expected) as well as off the equator at 4°N and 5°N in profiles from three cruise transects at 110°W through TIWs (Table 1; Figure 13). We estimate  $Ri$  by first averaging the 1 m binned CTD data in the bins used for the ADCP data (either 8 m or 10 m bins), and then estimating  $N^2$  and  $S^2$  using centered differences so the gradients are calculated over 16 m to 20 m. Bins where  $N^2 < 10^{-6} \text{ s}^{-2}$  and  $S^2 < 10^{-6} \text{ s}^{-2}$  are excluded. These  $Ri$  profiles are presented in Figure 13b,c,e,f,h,i along with a higher-resolution  $N^2$  profile estimated using 3 m averaged CTD profiles. In general,  $Ri < 1$  off the equator with values close to 0.25 in three to five successive bins below the mixed layer (where  $N^2 \approx 10^{-5} - 10^{-4} \text{ s}^{-2}$ , Figure 13c,f,i). As in the model,  $v_z$  is the dominant shear term (not shown). The data in Figure 13 are noisy but suggest that further examination of such sections might be useful given the lack of moored ADCPs and microstructure data. A more thorough analysis would use all sections at 110°W, 125°W and 140°W to estimate a median  $Ri$  profile through the TIW cold cusp. This work is ongoing.

## 6. Summary

We have presented evidence from a high-resolution numerical simulation that TIWs force a deep cycle of turbulence off the equator throughout the cold tongue (Figures 2, 4, 5, 3, 11). Horizontal vortex stretching by meridional diffluence  $v_y$  of the TIW's flow intensifies pre-existing  $u_z$  within approximately 2° of the equator (Figure 9c; Holmes

and Thomas 2015). The TIW's anticyclonic flow then rotates the horizontal vorticity anticyclonically while moving fluid away from the equator, converting  $u_z$  to  $v_z$  in the eastward extension of the cold cusp (Figures 8 and 9g,h). Flow deformation in the  $x - y$  plane also acts to modify the horizontal vorticity in the cold cusp. This continuous stretching and tilting of horizontal vorticity acts to create a region of intense shear and low  $Ri$  below the mixed layer in the TIW cold cusp (Figure 6). The flow regime in the TIW cold cusp is similar to the equatorial flow regime where intense shear ( $u_z$ ) between the SEC and EUC exists below the mixed layer, except that the shear is now associated with meridional flow ( $v_z$ , Figure 7). There is a daily cycle of turbulence in the off-equatorial low  $Ri$  layer that is associated with a downward descending shear layer in the afternoon (Figure 5).

Although the off-equatorial deep cycle has many qualitative similarities to the equatorial deep cycle, many details about the dynamics differ in the model. Notably the descending surface boundary layer, which triggers the deep cycle, always descends with the Monin-Obukhov (MO) depth  $L_{MO}$  as the stabilizing surface buoyancy flux weakens in the afternoon. At the equator, in contrast, the descent of the stable surface boundary layer during the afternoon is usually (approximately two-thirds of the time) controlled by the bulk Richardson number, that is increasing momentum in the near-surface layer, or occurs with the onset of convection in the evening (as in Large and Gent 1999; Pham et al. 2017). The descent of the surface boundary layer with  $L_{MO}$  occurs approximately one-third of the time. In any case, the deepening boundary layer results in mixing in the low  $Ri$  layer beneath the MLD leading to daily cycles of parameterized turbulence,  $Ri$ ,  $S^2$  and  $N^2$  in the low  $Ri$  layer in the cold cusp off the equator (Figures 5 and 11; Section d). Approximately one third of the simulated off-equatorial turbulent heat flux is within the surface boundary layer, in contrast to the equatorial deep-cycle which occurs exclusively below the boundary layer (Figure 11).

The accuracy of KPP's simulation of these details of the off-equatorial deep cycle needs to be evaluated with LES simulations that account for the large-scale lateral TIW shear forcing. Most published LES simulations of deep cycle turbulence do not account for lateral momentum and buoyancy flux forcing terms, and none that we know of account for TIW forcing explicitly. Observational evidence for an off-equatorial deep cycle is restricted to a small number of  $Ri$  profiles from opportunistic cruise transect data within a TIW cold cusp (Figure 13). Similarly the horizontal vortex stretching and tilting dynamics described here and in Holmes and Thomas (2015) also need to observationally verified. Hence, there is a need for high-resolution microstructure observations to validate the current MITgcm and future LES simulations.

The deep cycle transports heat absorbed by the near-surface ocean during daytime to depths deeper than the base of the convective mixed layer; keeping it away from reabsorption by the atmosphere during convection the following night. In doing so, the deep cycle helps keep the sea surface cool, enabling significant heat uptake by the eastern equatorial Pacific cold tongue while it remains in approximate thermal equilibrium. Our simulations indicate that this effective subduction of heat is taking place over an area larger than what might be expected from shear turbulence associated with SEC-EUC shear i.e. poleward of the  $3^{\circ}\text{S}$ - $3^{\circ}\text{N}$  region. Yet direct microstructure measurements have mostly been made at the equator. Our results, and the associated uncertainties, emphasize the need to constrain the magnitude, the dynamics, and the long term impact of off-equatorial turbulence in the eastern Pacific cold tongue.

**Acknowledgments.** This work was funded by National Oceanic and Atmospheric Administration Contract NA18OAR4310408 from the Climate Program Office. The MITgcm simulation output used for this paper is available on NCAR's GLADE storage system (A DOI will be provided during revisions). We acknowledge many fruitful discussions with Dr. Frank Bryan and Dr. Anna-Lena Deppenmeier. We would like to acknowledge high-performance computing support from Cheyenne (doi:10.5065/D6RX99HX) provided by NCAR's Computational and Information Systems Laboratory, sponsored by the National Science Foundation. Analysis was greatly helped by the use of the xarray Python package (Hoyer and Hamman 2017).

## References

- Adcroft, A., C. N. Hill, J.-M. Campin, J. Marshall, and P. Heimbach, 2004: Overview of the formulation and numerics of the MIT GCM. Tech. rep., 11 pp.
- Chelton, D. B., F. J. Wentz, C. L. Gentemann, R. A. de Szoeke, and M. G. Schlax, 2000: Satellite microwave SST observations of transequatorial tropical instability waves. *Geophys. Res. Lett.*, **27** (9), 1239–1242, doi:10/dqtvwj.
- Computational And Information Systems Laboratory, 2019: Cheyenne: SGI ICE XA Cluster (Climate Simulation Laboratory). Boulder, CO: National Center for Atmospheric Research. doi:10.5065/D6RX99HX.
- Dutrieux, P., C. E. Menkes, J. Vialard, P. Flament, and B. Blanke, 2008: Lagrangian Study of Tropical Instability Vortices in the Atlantic. *J. Phys. Oceanogr.*, **38** (2), 400–417, doi:10/dqmv9g.
- Gregg, M. C., H. Peters, J. C. Wesson, N. S. Oakey, and T. J. Shay, 1985: Intensive measurements of turbulence and shear in the equatorial undercurrent. *Nature*, **318** (6042), 140–144, doi:10.1038/318140a0.
- Holmes, R. M., and L. N. Thomas, 2015: The Modulation of Equatorial Turbulence by Tropical Instability Waves in a Regional Ocean Model. *J. Phys. Oceanogr.*, **45** (4), 1155–1173, doi:10/f68n4x.

- Holmes, R. M., and L. N. Thomas, 2016: Modulation of Tropical Instability Wave Intensity by Equatorial Kelvin Waves. *J. Phys. Oceanogr.*, **46** (9), 2623–2643, doi:10/f85nws.
- Holmes, R. M., L. N. Thomas, L. Thompson, and D. Darr, 2014: Potential Vorticity Dynamics of Tropical Instability Vortices. *J. Phys. Oceanogr.*, **44** (3), 995–1011, doi:10/f5vw3q.
- Holmes, R. M., J. D. Zika, and M. H. England, 2019: Diathermal Heat Transport in a Global Ocean Model. *J. Phys. Oceanogr.*, **49** (1), 141–161, doi:10/gfs9z9.
- Hoyer, S., and J. J. Hamman, 2017: Xarray: N-D labeled Arrays and Datasets in Python. *J. Open Res. Softw.*, **5**, doi:10.5334/jors.148.
- Inoue, R., R. Lien, J. N. Moum, R. C. Perez, and M. C. Gregg, 2019: Variations of Equatorial Shear, Stratification, and Turbulence Within a Tropical Instability Wave Cycle. *J. Geophys. Res. Oceans*, doi:10/gfxzhc.
- Inoue, R., R.-C. Lien, and J. N. Moum, 2012: Modulation of equatorial turbulence by a tropical instability wave. *J. Geophys. Res. Oceans*, **117** (C10), n/a–n/a, doi:10/gfxzg5.
- Johnson, G. C., B. M. Sloyan, W. S. Kessler, and K. E. McTaggart, 2002: Direct measurements of upper ocean currents and water properties across the tropical Pacific during the 1990s. *Prog. Oceanogr.*, **52** (1), 31–61, doi:10.1016/S0079-6611(02)00021-6.
- Kennan, S. C., and P. J. Flament, 2000: Observations of a Tropical Instability Vortex. *J. Phys. Oceanogr.*, **30** (9), 2277–2301, doi:10/bjjm2g.
- Large, W. G., and P. R. Gent, 1999: Validation of Vertical Mixing in an Equatorial Ocean Model Using Large Eddy Simulations and Observations. *J. Phys. Oceanogr.*, **29** (3), 449–464, doi:10/d5xf5p.
- Large, W. G., J. C. McWilliams, and S. C. Doney, 1994: Oceanic vertical mixing: A review and a model with a nonlocal boundary layer parameterization. *Rev. Geophys.*, **32** (4), 363, doi:10.1029/94RG01872.
- Large, W. G., and S. G. Yeager, 2009: The global climatology of an interannually varying air-sea flux data set. *Clim. Dyn.*, **33** (2-3), 341–364, doi:10/dnz36q.
- Legeckis, R., 1977: Long Waves in the Eastern Equatorial Pacific Ocean: A View from a Geostationary Satellite. *Science*, **197** (4309), 1179–1181, doi:10/bjmsrj.
- Lien, R.-C., D. R. Caldwell, M. C. Gregg, and J. N. Moum, 1995: Turbulence variability at the equator in the central Pacific at the beginning of the 1991–1993 El Niño. *J. Geophys. Res.*, **100** (C4), 6881, doi:10.1029/94JC03312.
- Lien, R.-C., E. A. D’Asaro, and C. E. Menkes, 2008: Modulation of equatorial turbulence by tropical instability waves. *Geophys. Res. Lett.*, **35** (24), doi:10/fcvdgw.
- Liu, C., L. Fang, A. Köhl, Z. Liu, W. D. Smyth, and F. Wang, 2019: The Subsurface Mode Tropical Instability Waves in the Equatorial Pacific Ocean and Their Impacts on Shear and Mixing. *Geophys. Res. Lett.*, **46** (21), 12 270–12 278, doi:10/gg4vwz.
- Liu, C., X. Wang, Z. Liu, A. Köhl, W. D. Smyth, and F. Wang, 2020: On the formation of a subsurface weakly sheared laminar layer and an upper thermocline strongly sheared turbulent layer in the eastern equatorial Pacific: Interplays of multiple time scale equatorial waves. *J. Phys. Oceanogr.*, 1–48, doi:10/gg9n83.
- Lyman, J. M., D. B. Chelton, R. A. deSzoeke, and R. M. Samelson, 2005: Tropical Instability Waves as a Resonance between Equatorial Rossby Waves\*. *J. Phys. Oceanogr.*, **35** (2), 232–254, doi:10.1175/JPO-2668.1.
- Marshall, J., A. Adcroft, C. Hill, L. Perelman, and C. Heisey, 1997: A finite-volume, incompressible Navier Stokes model for studies of the ocean on parallel computers. *J. Geophys. Res. Oceans*, **102** (C3), 5753–5766, doi:10/fs467q.
- Menkes, C. E. R., J. G. Vialard, S. C. Kennan, J.-P. Boulanger, and G. V. Madec, 2006: A Modeling Study of the Impact of Tropical Instability Waves on the Heat Budget of the Eastern Equatorial Pacific. *J. Phys. Oceanogr.*, **36** (5), 847–865, doi:10/fwff6x.
- Moum, J. N., and D. R. Caldwell, 1985: Local Influences on Shear-Flow Turbulence in the Equatorial Ocean. *Science*, **230** (4723), 315–316, doi:10/crxwt.
- Moum, J. N., R.-C. Lien, A. Perlin, J. D. Nash, M. C. Gregg, and P. J. Wiles, 2009: Sea surface cooling at the Equator by subsurface mixing in tropical instability waves. *Nat. Geosci.*, **2** (11), 761–765, doi:10.1038/ngeo657.
- Moum, J. N., A. Perlin, J. D. Nash, and M. J. McPhaden, 2013: Seasonal sea surface cooling in the equatorial Pacific cold tongue controlled by ocean mixing. *Nature*, **500** (7460), 64–67, doi:10.1038/nature12363.
- Pei, S., T. Shinoda, W. Wang, and R. Lien, 2020: Simulation of Deep Cycle Turbulence by a Global Ocean General Circulation Model. *Geophys. Res. Lett.*, **47** (15), doi:10/gg7vm9.
- Peters, H., M. C. Gregg, and T. B. Sanford, 1994: The diurnal cycle of the upper equatorial ocean: Turbulence, fine-scale shear, and mean shear. *J. Geophys. Res.*, **99** (C4), 7707, doi:10/bmh9bm.
- Peters, H., M. C. Gregg, and J. M. Toole, 1988: On the parameterization of equatorial turbulence. *J. Geophys. Res.*, **93** (C2), 1199, doi:10/bczx9k.
- Pham, H. T., W. D. Smyth, S. Sarkar, and J. N. Moum, 2017: Seasonality of Deep Cycle Turbulence in the Eastern Equatorial Pacific. *J. Phys. Oceanogr.*, **47** (9), 2189–2209, doi:10/gb4t3m.
- Philander, S. G. H., 1976: Instabilities of zonal equatorial currents. *J. Geophys. Res.*, **81** (21), 3725–3735, doi:10/fj7h66.
- Pujiana, K., J. N. Moum, and W. D. Smyth, 2018: The Role of Turbulence in Redistributing Upper-Ocean Heat, Freshwater, and Momentum in Response to the MJO in the Equatorial Indian Ocean. *J. Phys. Oceanogr.*, **48** (1), 197–220, doi:10.1175/JPO-D-17-0146.1.
- Qiao, L., and R. H. Weisberg, 1995: Tropical instability wave kinematics: Observations from the Tropical Instability Wave Experiment. *J. Geophys. Res.*, **100** (C5), 8677, doi:10/ck2rw5.
- Ray, S., A. T. Wittenberg, S. M. Griffies, and F. Zeng, 2018: Understanding the Equatorial Pacific Cold Tongue Time-Mean Heat Budget. Part I: Diagnostic Framework. *J. Clim.*, **31** (24), 9965–9985, doi:10/gfp8vr.
- Reynolds, R. W., T. M. Smith, C. Liu, D. B. Chelton, K. S. Casey, and M. G. Schlax, 2007: Daily High-Resolution-Blended Analyses for Sea Surface Temperature. *J. Clim.*, **20** (22), 5473–5496, doi:10/bzjh5f.
- Smyth, W. D., and J. N. Moum, 2013: Marginal instability and deep cycle turbulence in the eastern equatorial Pacific Ocean. *Geophys. Res. Lett.*, **40** (23), 6181–6185, doi:10.1002/2013GL058403.

- Smyth, W. D., J. N. Moum, L. Li, and S. A. Thorpe, 2013: Diurnal Shear Instability, the Descent of the Surface Shear Layer, and the Deep Cycle of Equatorial Turbulence. *J. Phys. Oceanogr.*, **43** (11), 2432–2455, doi:10/gf3w8k.
- Smyth, W. D., J. D. Nash, and J. N. Moum, 2019: Self-organized criticality in geophysical turbulence. *Sci. Rep.*, **9** (1), doi:10/gfxzg8.
- Strutton, P. G., J. P. Ryan, and F. P. Chavez, 2001: Enhanced chlorophyll associated with tropical instability waves in the equatorial Pacific. *Geophys. Res. Lett.*, **28** (10), 2005–2008, doi:10/bxvdf3.
- Thorpe, S. A., and Z. Liu, 2009: Marginal Instability? *J. Phys. Oceanogr.*, **39** (9), 2373–2381, doi:10/cb7rph.
- Tsujino, H., and Coauthors, 2018: JRA-55 based surface dataset for driving ocean-sea-ice models (JRA55-do). *Ocean Model.*, **130**, 79–139, doi:10/gfcvn6.
- Wang, W., and M. J. McPhaden, 1999: The Surface-Layer Heat Balance in the Equatorial Pacific Ocean. Part I: Mean Seasonal Cycle\*. *J. Phys. Oceanogr.*, **29** (8), 1812–1831, doi:10/bmf6ps.
- Wang, W., and M. J. McPhaden, 2000: The Surface-Layer Heat Balance in the Equatorial Pacific Ocean. Part II: Interannual Variability\*. *J. Phys. Oceanogr.*, **30** (11), 2989–3008, doi:10/cjm35f.
- Warner, S. J., R. M. Holmes, E. H. M. Hawkins, M. S. Hoecker-Martínez, A. C. Savage, and J. N. Moum, 2018: Buoyant Gravity Currents Released from Tropical Instability Waves. *J. Phys. Oceanogr.*, **48** (2), 361–382, doi:10.1175/JPO-D-17-0144.1.
- Warner, S. J., and J. N. Moum, 2019: Feedback of Mixing to ENSO Phase Change. *Geophys. Res. Lett.*, **46** (23), 13 920–13 927, doi:10/ggsqcw.
- Wenegrat, J. O., and M. J. McPhaden, 2015: Dynamics of the surface layer diurnal cycle in the equatorial Atlantic Ocean ( $0^{\circ}$ ,  $23^{\circ}\text{W}$ ). *J. Geophys. Res. Oceans*, **120** (1), 563–581, doi:10.1002/2014JC010504.
- Wijesekera, H. W., and T. M. Dillon, 1991: Internal waves and mixing in the upper equatorial Pacific Ocean. *J. Geophys. Res.*, **96** (C4), 7115, doi:10/dc7w9g.
- Yoder, J. A., S. G. Ackleson, R. T. Barber, P. Flament, and W. M. Balch, 1994: A line in the sea. *Nature*, **371** (6499), 689–692, doi:10/cpc6t3.
- Zaron, E. D., and J. N. Moum, 2009: A New Look at Richardson Number Mixing Schemes for Equatorial Ocean Modeling. *J. Phys. Oceanogr.*, **39** (10), 2652–2664, doi:10/cphgzg.

Table 1. Cruise sections at 110°W used for analysis in Section 5

Cruise	Vessel	Dates	Sampling Line	ADCP bin size
EP692	<i>R/V Discoverer</i>	1992/10/15 – 1992/11/19	WOCE PR16	10 m
EP393	<i>R/V Discoverer</i>	1993/08/24 – 1993/09/18	WOCE PR16	8 m
RB0711	<i>R/V Ron Brown</i>	2007/12/15 – 2008/01/18	CLIVAR P18N	8 m

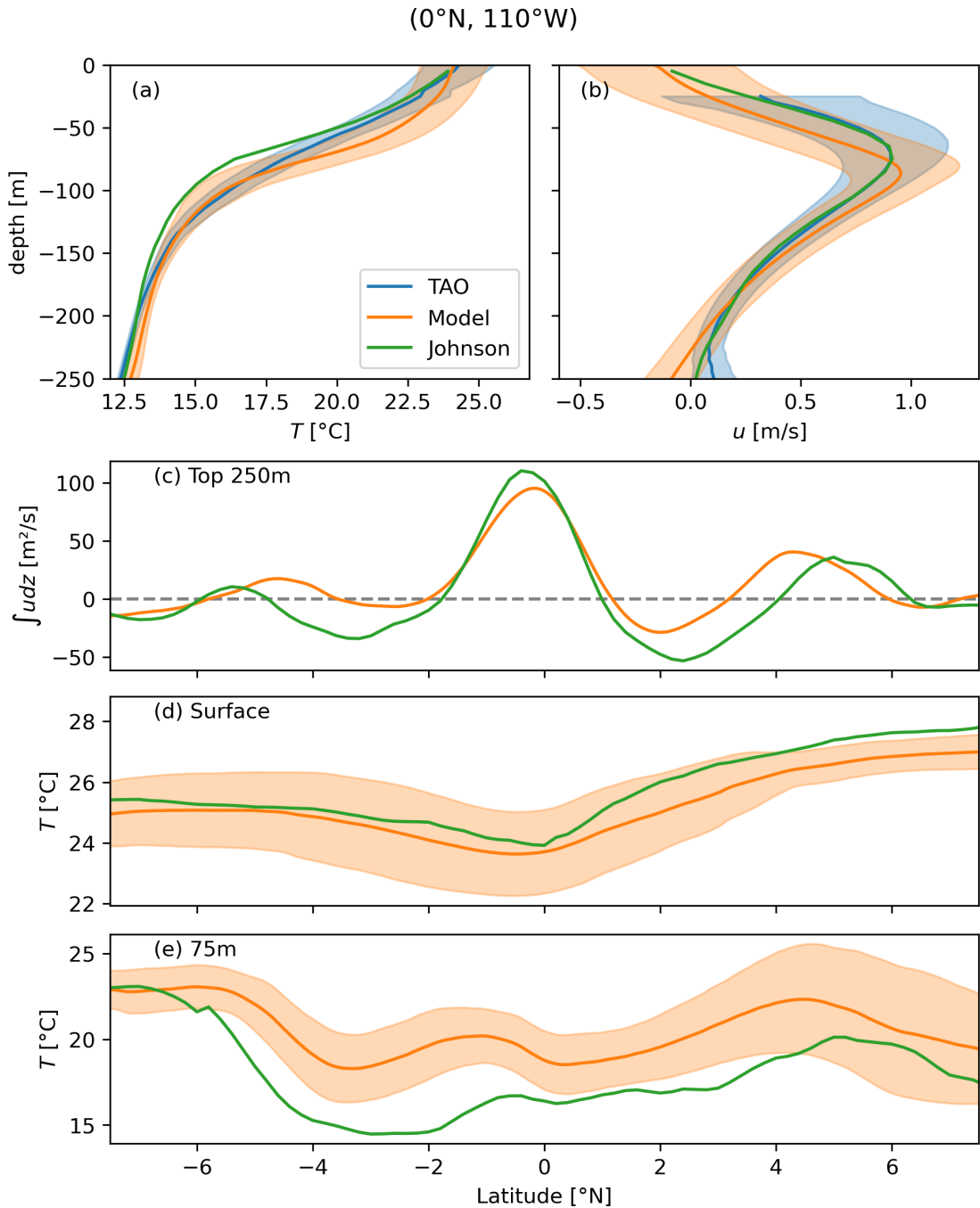


Figure 1. Comparisons between modeled and observed zonal velocity and temperature at 110°W. (a,b) Annual mean fields (solid line) and standard deviation of daily means over a year (shaded) for three datasets: the model during 1996 (orange), a climatological annual cycle constructed from the TAO dataset between 1990 and 2000 (blue), and the Johnson et al. (2002) climatology (green, no standard deviation available). (c) Vertically integrated zonal velocity in the top 250m from the model and the Johnson dataset. (d, e) Meridional section of temperature at (d) the surface and (e) 75m.

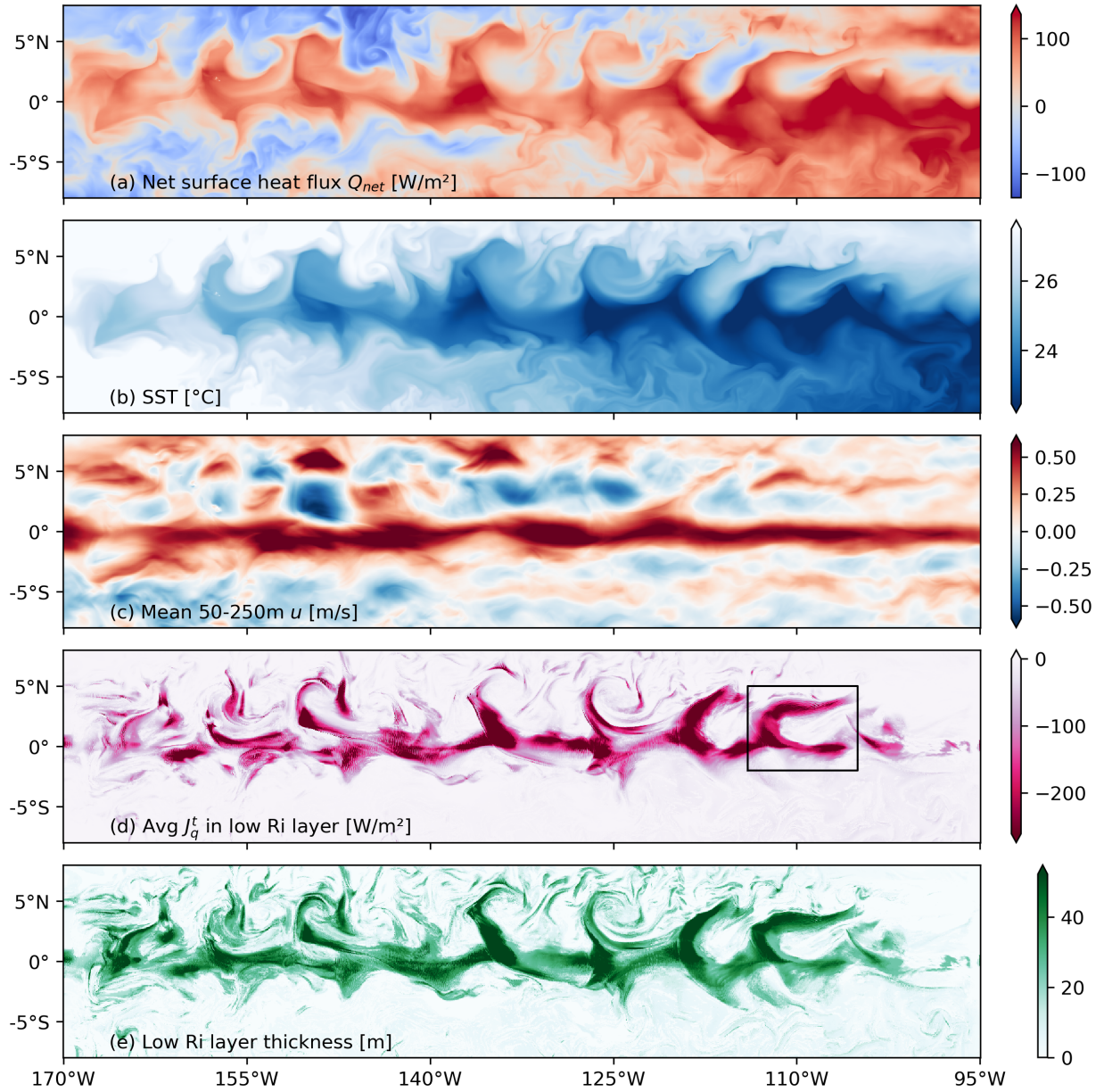


Figure 2. Daily averaged fields for 05 Dec 1995. (a) Net surface heat flux  $Q_{\text{net}}$  (positive means heat enters the ocean). (b) SST. (c) Mean zonal velocity between 50- and 250-m. (d) Integrated turbulent heat flux in the low Ri layer ( $z_{\text{Ri}} \leq z < z_{\text{MLD}}$ ) normalized by a depth of 50m (e) Thickness of the low Ri layer ( $z_{\text{MLD}} - z_{\text{Ri}}$ ). The black rectangle in (d) marks the TIW that is studied in detail later in this paper (e.g. Figure 4).

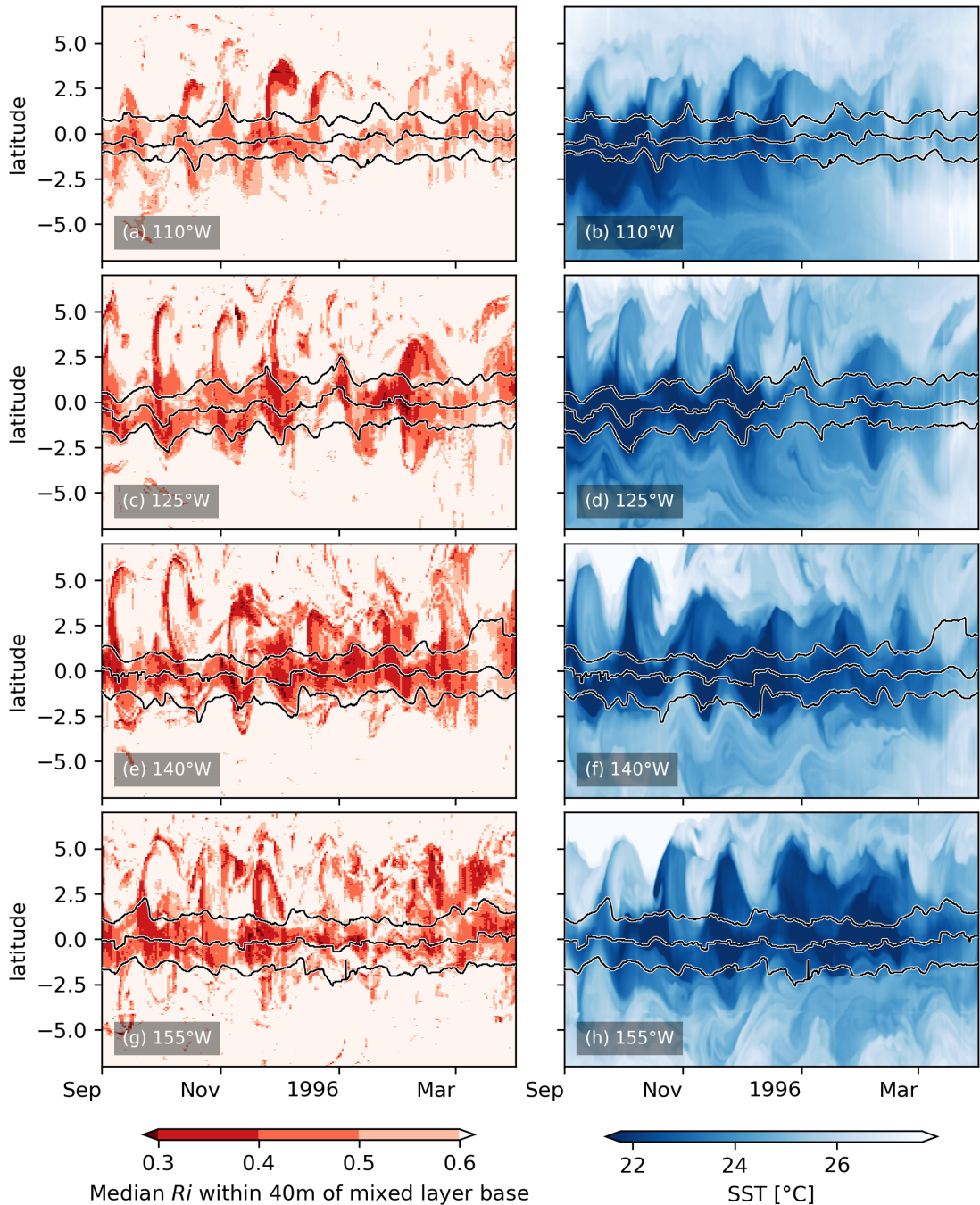


Figure 3. Low  $Ri$  seen in the off-equatorial region at  $110^{\circ}\text{W}$ ,  $125^{\circ}\text{W}$ ,  $140^{\circ}\text{W}$ ,  $155^{\circ}\text{W}$  (rows) between September 1995 and March 1996. (left column) Median  $Ri$  in the region  $z_{\text{MLD}} - 40 \leq z \leq z_{\text{MLD}}$  (right) Daily averaged SST illustrating TIW activity. Black lines on all panels show the EUC maximum and its latitudinal extent defined using the latitudes north and south of the core at which the eastward velocity drops by a factor of 2. The latitudes are determined using  $u$  at the depth of maximum eastward velocity.

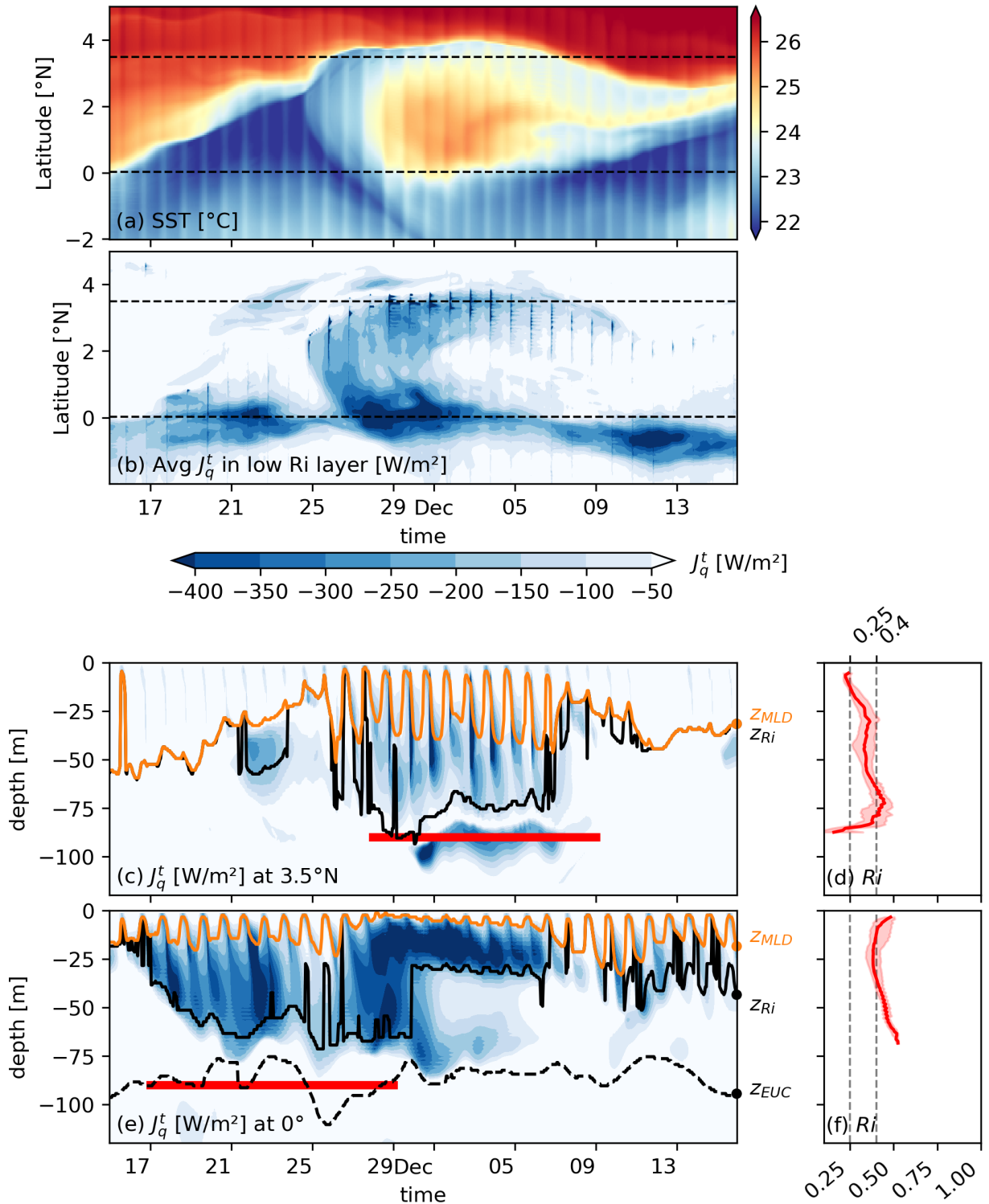


Figure 4. Deep cycle turbulence at the equator and  $3.5^{\circ}\text{N}$ . (a, b) Time-latitude plots of (a) SST, and (b) KPP heat flux  $J_q^t$ . (c, e) Time-depth plots of KPP heat flux  $J_q^t$ . (d, f) Median (solid line) and interquartile range (shading) of  $Ri$  in the low  $Ri$  layer  $z_{\text{Ri}} \leq z \leq z_{\text{MLD}}$  for the time period marked by red horizontal lines in panels (c, e) respectively. Dashed vertical lines in (d, f) mark  $Ri = 0.25$  and  $Ri = 0.4$ .

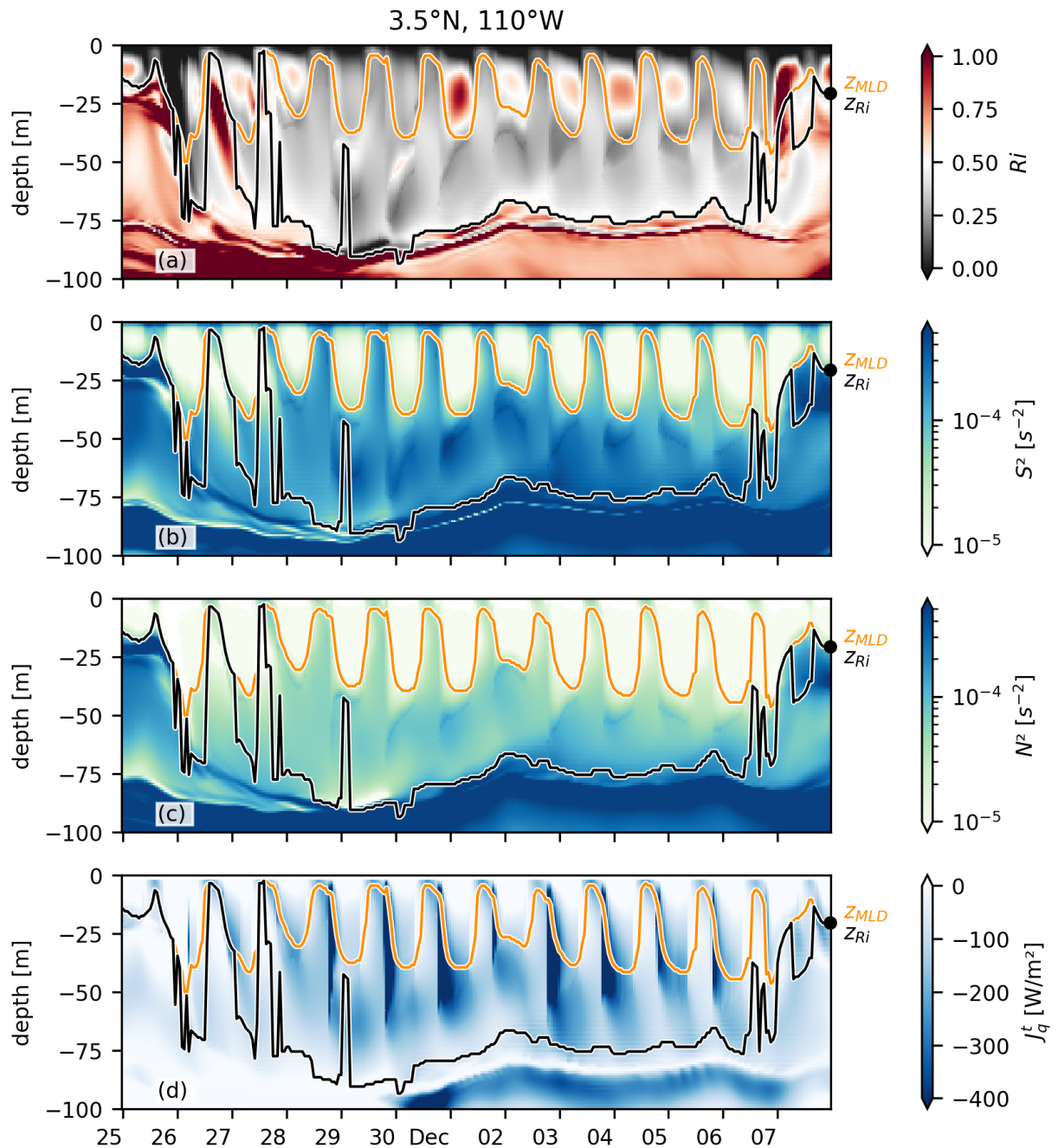


Figure 5. Daily cycles in (a)  $Ri$ , (b) squared shear  $S^2$ , (c) buoyancy frequency  $N^2$ , and (d)  $J_q^t$  at  $3.5^\circ\text{N}$ . This time period is a subset of the time period shown in Figure 4. Also shown are the mixed layer depth  $z_{MLD}$  (orange line) and the depth of the base of the low  $Ri$  layer  $z_{Ri}$  (black line).

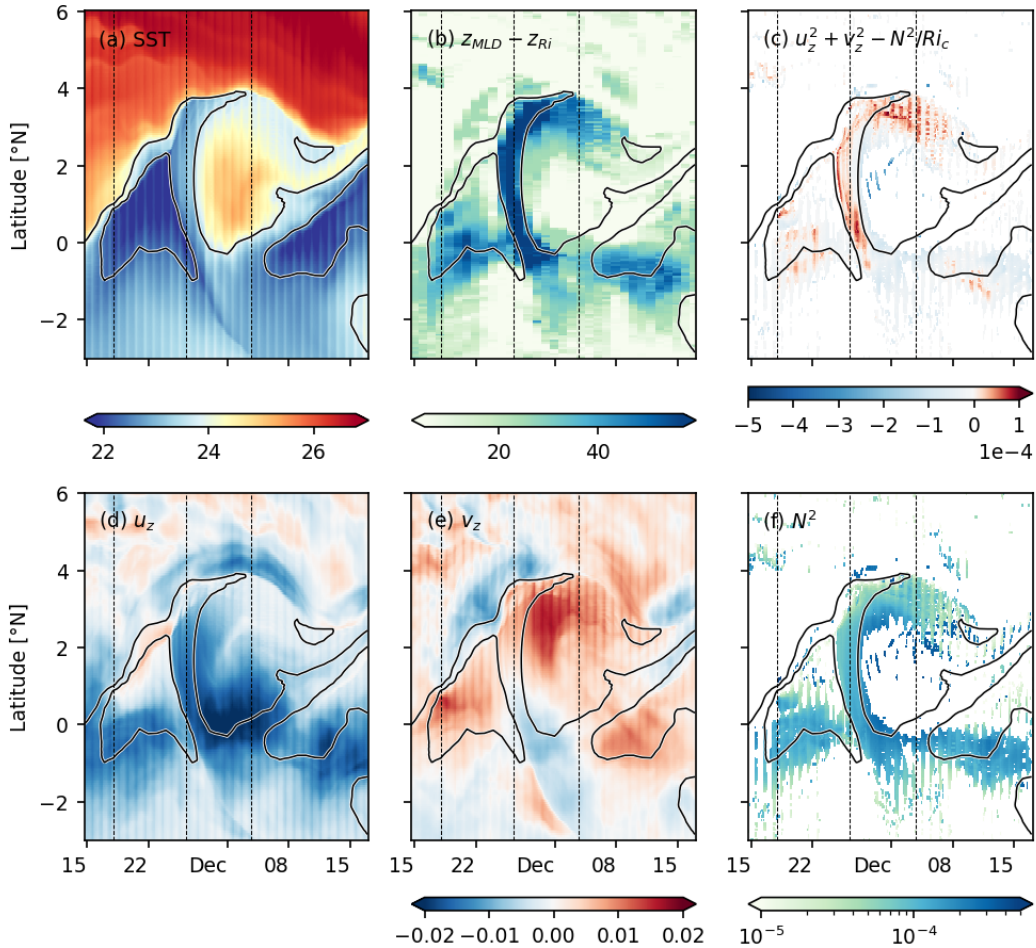


Figure 6. Time-latitude plots of (a) SST, (b) low Ri layer thickness, (c) median  $Sh_{red}^2$  within the low Ri layer (same colorbar as in Figure 7), (d) mean  $u_z$  in the top 60 m, (e) mean  $v_z$  in the top 60 m, and (f) mean  $N^2$  within the low Ri layer for one TIW. Vertical lines mark time instants presented in Figure 7. The black contours mark SSTs of 22.4°C and 23.5 C.

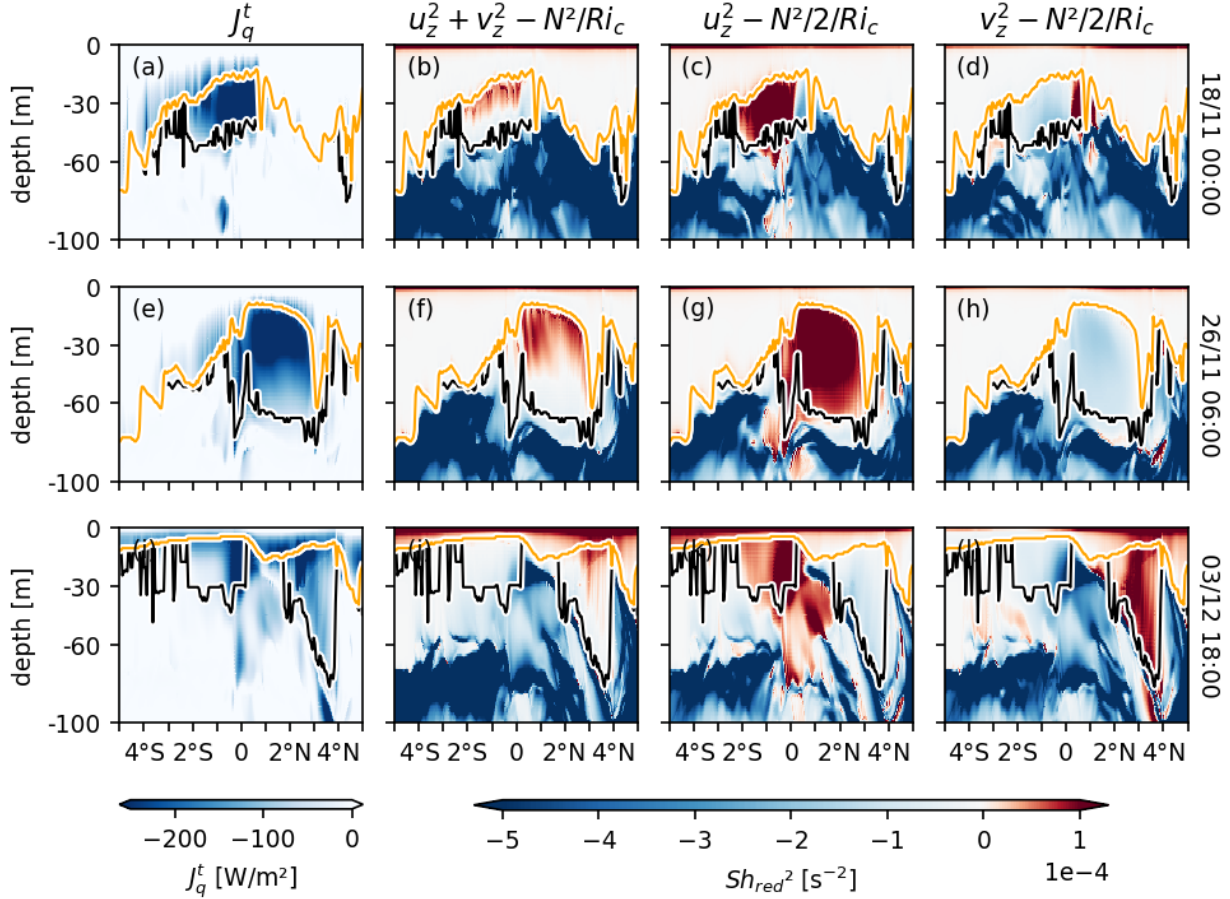


Figure 7. Zonal shear drives enhanced equatorial turbulence while meridional shear drives enhanced off-equatorial turbulence. In both cases, the turbulence is in the low  $Ri$  layer. (a, e, i) Turbulent heat flux  $J_q^t$ ; (b, f, j) reduced shear  $Sh_{red}^2$ ; and contributions to  $Sh_{red}^2$  from (c, g, k) zonal shear and (d, h, l) meridional shear (see equation 5) as a function of depth and latitude at three different time instants. These time instants, indicated on the right of each row of plots, are (top) prior to the arrival of the cold cusp, (middle) when the cold cusp is oriented northward, and (bottom) when the cold cusp extends eastward. The time instants are also marked by vertical lines in Figure 6.  $z_{MLD}$  and  $z_{Ri}$  are marked by orange and black lines respectively.

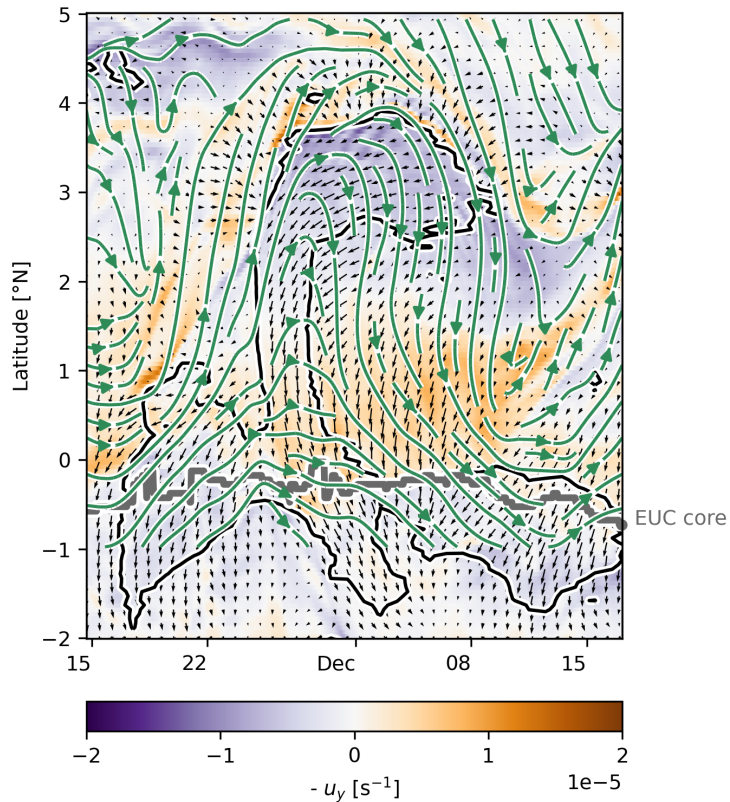


Figure 8. Depth-averaged horizontal vorticity vectors  $\omega^x \hat{i} + \omega^y \hat{j} = (w_y - v_z) \hat{i} + (u_z - w_x) \hat{j}$  (black vectors) over depth-averaged  $-u_y$  (color). Streamlines, in green, are calculated using depth-averaged horizontal velocities with a TIW westward translation speed of  $0.5 m s^{-1}$  removed. All quantities are depth averaged to 60 m. The daily averaged SST =  $23.8^{\circ}C$  contour is shown in black. The latitude of the EUC core (defined as maximum  $u$  averaged between 30 m and 120 m) is marked in gray. The horizontal vorticity vector rotates as parcels travel northward from the equator and then eastward.

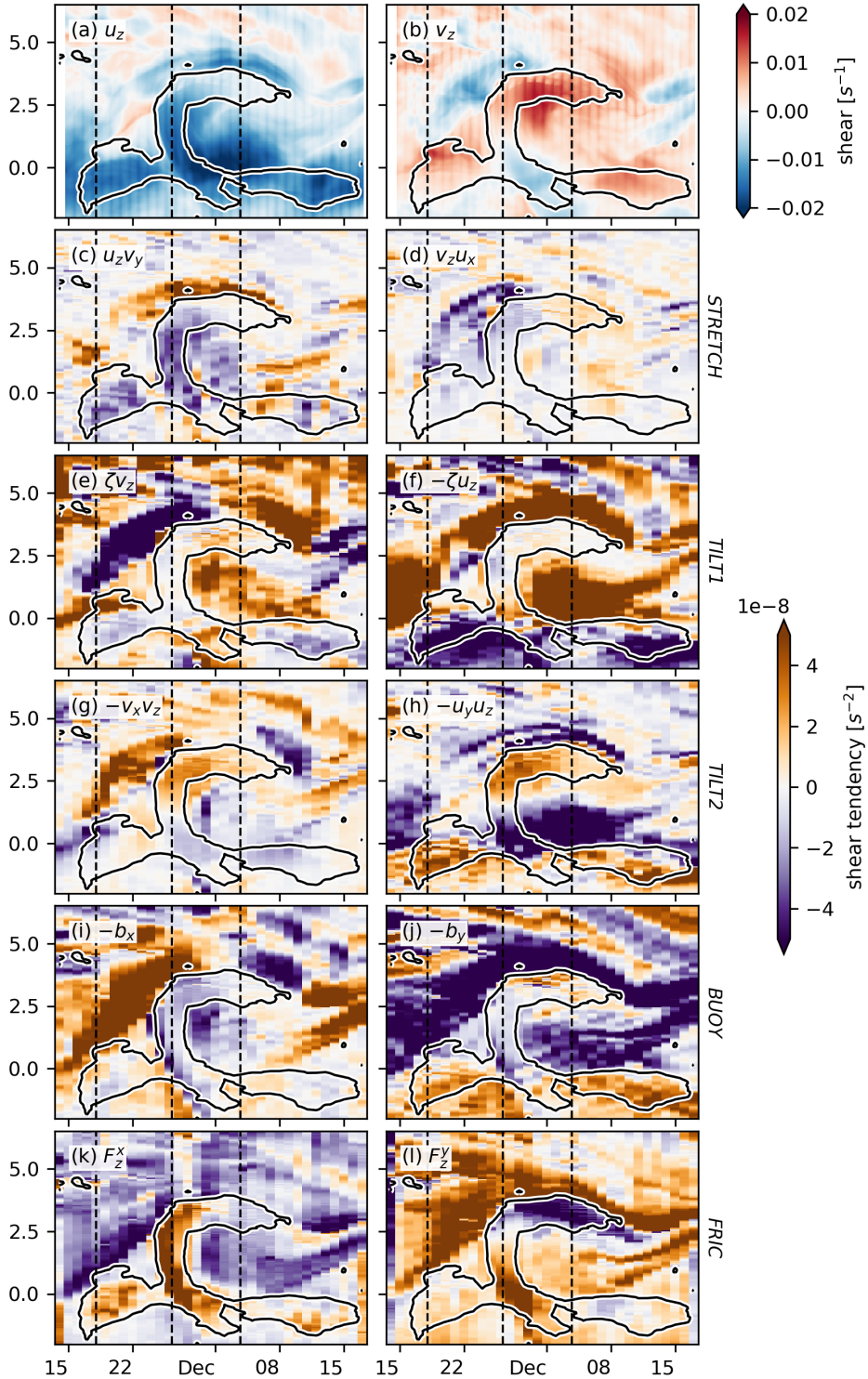


Figure 9. Terms controlling the evolution of  $u_z$  (left column, equation (6)) and  $v_z$  (right column, equation (7)). All quantities are depth-averaged in the top 60m. Black contours mark the low Ri layer thickness of 30 m for reference. Vertical lines mark the same timestamps as those in Figure 7.

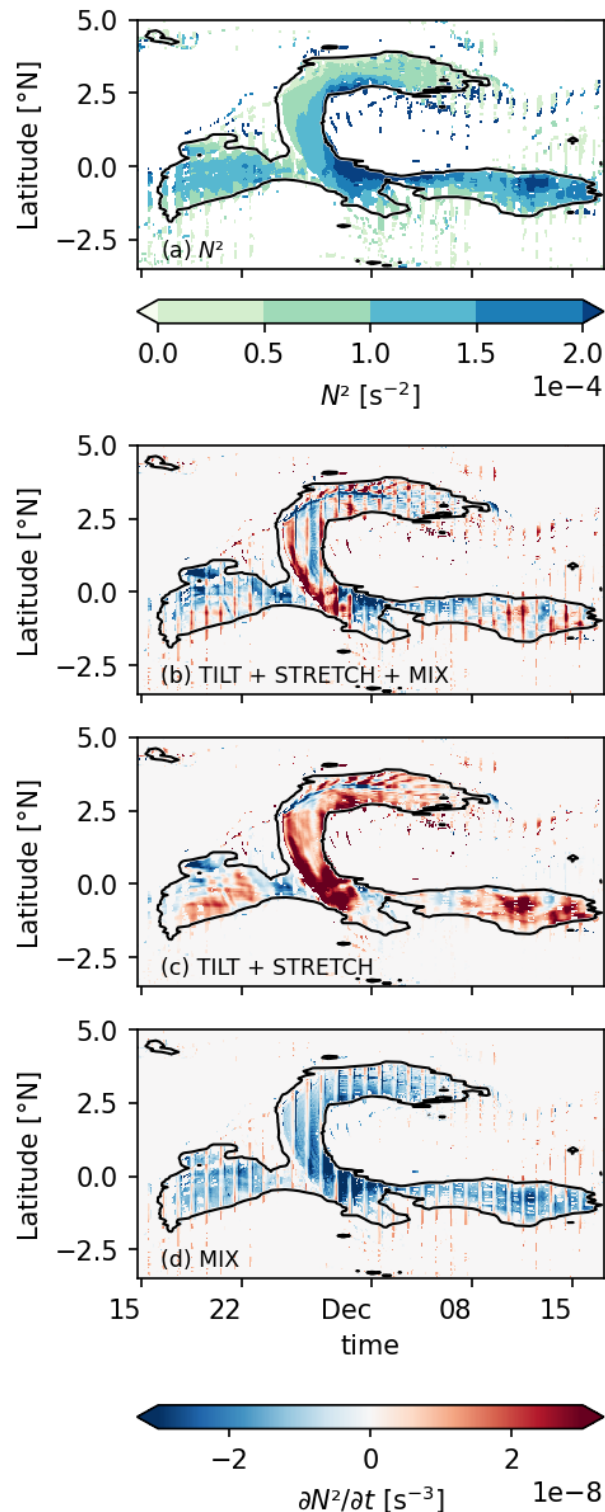


Figure 10. Time-latitude plots of (a)  $N^2$ , and (b–d) the stretching, tilting and mixing terms that contribute to  $\partial N^2 / \partial t$  (from equation 9) within the low Ri layer. The low Ri layer thickness is larger than 30 m within the black contour.

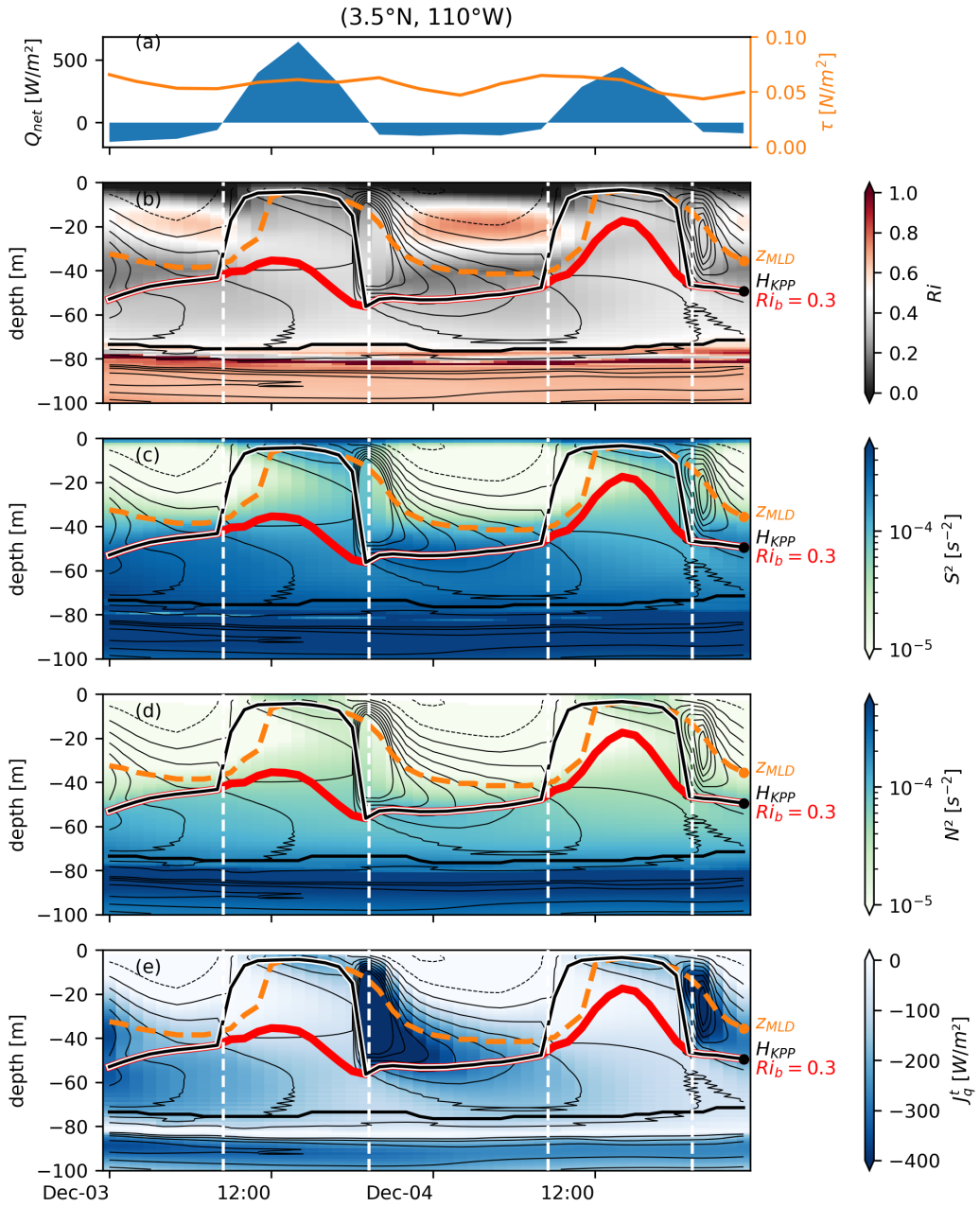


Figure 11. Turbulence at 3.5°N, 110°W triggered by deepening of the boundary layer in the afternoon. (a) Surface forcing with net surface heat flux in blue and wind stress in orange. (b) Gradient  $Ri$ , (c)  $S^2$ , (d)  $N^2$ , and (e) Turbulent heat flux  $J_q^t$ . Panels (b-e) also show the turbulent heat flux  $J_q^t$  (black contours; solid lines are negative, dashed are positive), the mixed layer depth ( $z_{MLD}$ , orange dashed line), the KPP boundary layer depth (black line), and the depth at which the bulk  $Ri_b$  reaches 0.3 ( $H_{0.3}$ , red line). Vertical white dashed lines mark time at which net surface heat flux changes sign.

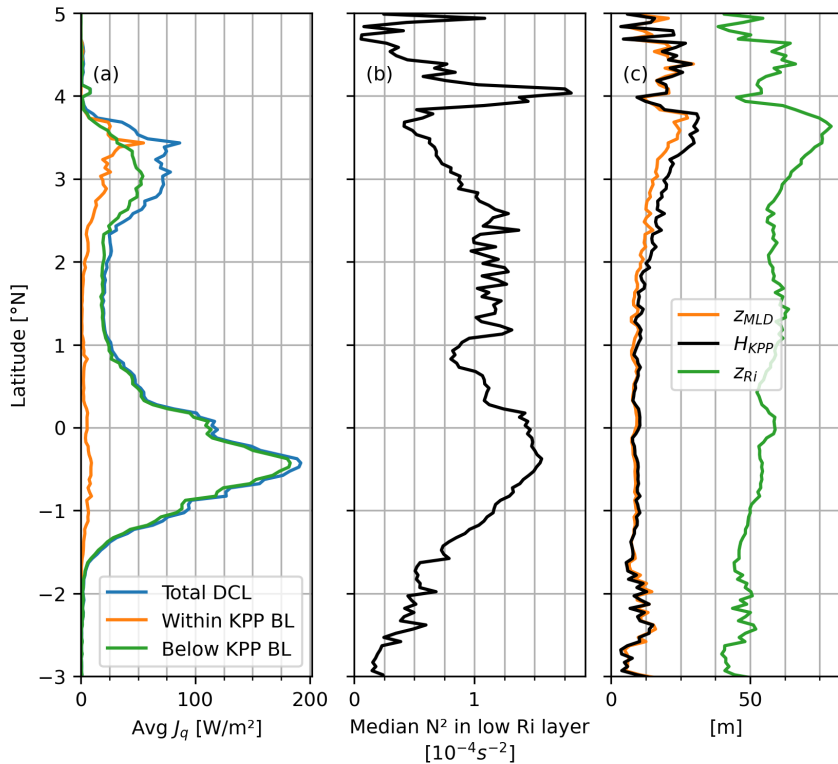


Figure 12. Meridional profiles of quantities averaged within the low Ri layer at 110°W during the duration of the TIW. (a)  $J_q^t$  averaged over time and depth. (b) Median  $N^2$  within the low Ri layer. The median is taken over time and depth axes. (c) Time-mean  $z_{MLD}$ ,  $H_{KPP}$  and  $z_{Ri}$  over the period when the deep cycle is active.

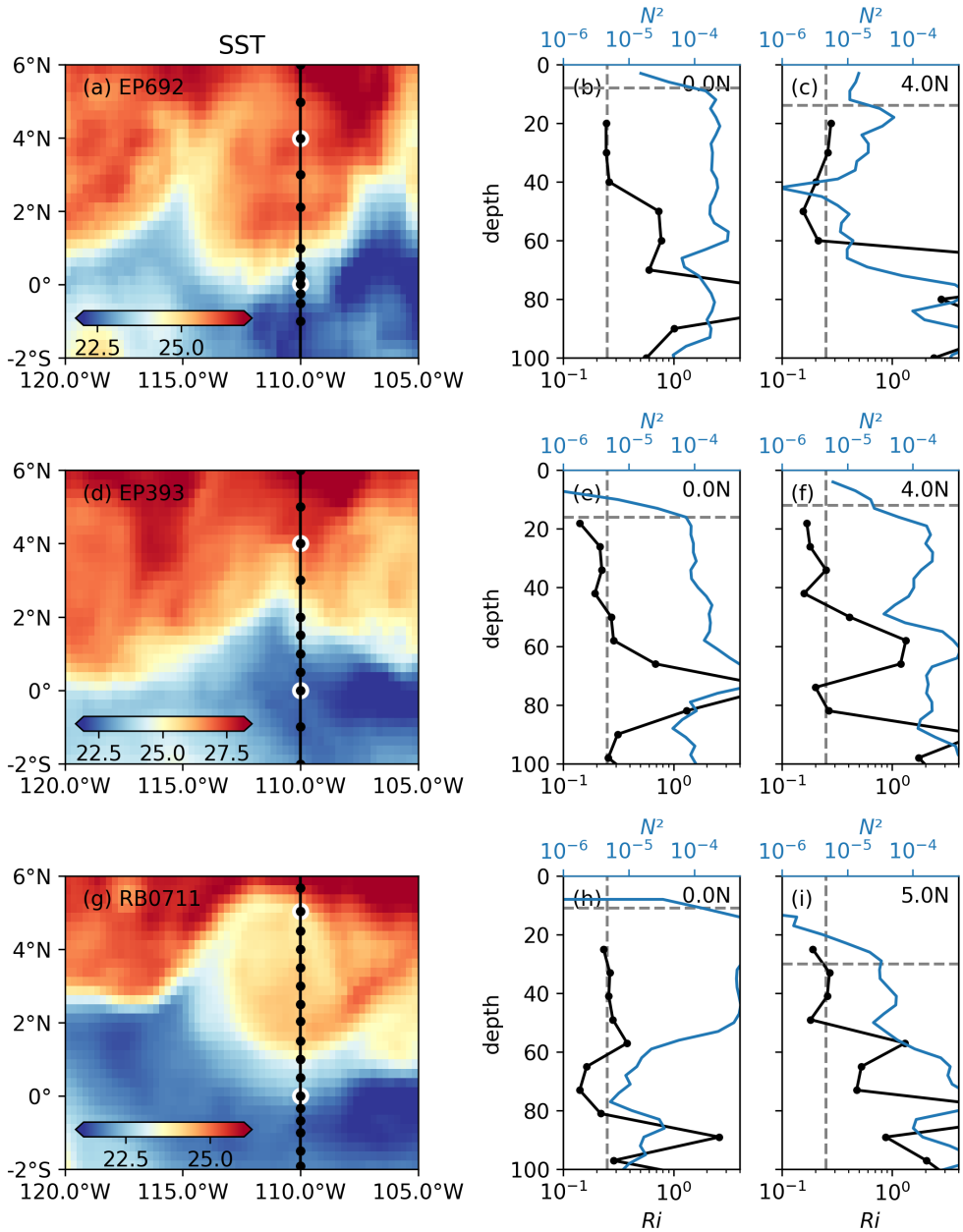


Figure 13. Indirect evidence for an off-equatorial deep cycle from three cruise transects (Table\* 1). (a,d,g) SST from the daily  $0.25^\circ$  OISST product (Reynolds et al. 2007) with CTD stations marked (note changing color scale). (b,c; e,f; h,i) Profiles of  $Ri$  (black) and  $N^2$  (blue) at stations marked with white circles in (a, d, g). The vertical line is  $Ri = 0.25$  and the horizontal line is mixed layer depth estimated as the shallowest depth at which the potential density exceeds the shallowest recorded density value by  $0.015 \text{ kg m}^{-3}$ .